The Electrochemical Society
Advancing solid state & electrochemical science & technology

Li Insertion in Ball Milled Si-Mn Alloys

View the article online for updates and enhancements.

Li Insertion in Ball Milled Si-Mn Alloys

Yidan Cao,[1,2] J. Craig Bennett,[3] R. A. Dunlap,[1,4,5] and M. N. Obrovac [1,2,4,*,z]

[1]*Department of Physics and Atmospheric Science, Dalhousie University, Halifax, Nova Scotia, Canada*
[2]*Department of Chemistry, Dalhousie University, Halifax, Nova Scotia, Canada*
[3]*Department of Physics, Acadia University, Wolfville, Nova Scotia, Canada*
[4]*Clean Technologies Research Institute, Dalhousie University, Halifax, Nova Scotia, Canada*
[5]*College of Sustainability, Dalhousie University, Halifax, Nova Scotia, Canada*

$Si_{1-x}Mn_x$ ($0 \leq x \leq 0.5$, $\Delta x = 0.05$) alloys were prepared by ball milling and studied as negative electrode materials in Li cells. These alloys were found to be unique among transition metals. When $x \leq 0.35$, the alloys are essentially homogeneous with nanocrystallites of $Si_{19}Mn_{11}$ uniformly dispersed in a matrix of amorphous silicon. Nanocrystallites of SiMn and $Si_{19}Mn_{11}$ coexist in samples with $x > 0.35$. The formation of $Li_{15}Si_4$ during lithiation was totally suppressed for alloys with $x \geq 0.3$. Cycling performance was significantly improved by Mn addition, especially for the samples in which the formation of $Li_{15}Si_4$ was suppressed. The addition of Mn increases the particle size, which results in reduced surface area. Capacity trends suggest that inactive $Si_{19}Mn_{11}$ and SiMn phases were formed in these alloys, consistent with XRD results. The $x = 0.25$ alloy achieved a volumetric capacity of 1526 Ah/L with 95% capacity retention after 50 cycles.

Si-based negative electrode materials for lithium-ion batteries have received considerable attention because of their high volumetric capacity (2194 Ah/L for Si, compared to 764 Ah/L for graphite).[1] Taking the delithiation voltage into consideration, Si can theoretically provide ∼34% energy density improvement over graphite in a full cell model.[2] Pure Si, however, suffers from severe volume changes (280% volume expansion in the fully lithiated state) during the lithiation/delithiation process.[3] This is detrimental to cycling performance because of the high internal stresses developed in the electrode, which can lead to particle fracture, the disruption of the solid electrolyte interphase (SEI) layer and the loss of electrical contact among the active particles in an electrode.[4,5] Incorporating Li-inactive elements with Si to form active/inactive alloys is one promising approach to mitigate these problems. The cycling of Si can be effectively improved by adding elements that suppress formation of $Li_{15}Si_4$, such as Zn, Ag, and Sn, or by reducing volume expansion by adding an inactive phase, such as Fe.[6–9]

Si-TM alloys (TM = a transition metal) have been extensively studied as negative electrodes to improve the cycling performance of silicon. When made by sputtering or ball milling, such alloys typically form active Si /inactive matrix nanostructured composites, where the inactive matrix comprises a transition metal silicide.[3,10] Transition metal silicides are theoretically active with lithium from a thermodynamic basis,[11] and $NiSi_2$ has been found to be active when it is ball milled to nano-grain sizes.[12] However, most transition metal silicides have been found to be completely inactive or have very limited capacity at room temperature.[3,13–16] Transition metals in alloys can facilitate the production of an amorphous/nanocrystalline state, reduce the overall volume change by limiting specific capacity, and suppress the formation of $Li_{15}Si_4$ during lithiation.[8,10,17] Among the transition metals, manganese is a promising candidate considering its low cost and abundance. It was found that the existence of Mn in the Si-Mn system was favorable to enhance the cycleability of active silicon.[8,18–20] Zuo et al. found that mechanically ball milled Si–Mn and Si-Mn-C composites have good cycling performance compared with pure silicon.[18,19] However, phase behavior was not clarified in their study and the capacity was limited to below 500 mAh/g. Thin films of Si-M (M = Mn, Fe, Cr+Ni) were fabricated by Fleischauer and Dahn.[8] They observed that the capacity decreases as transition metal content increases, and approaches zero at around 50 atom% Si.

This was explained by the reaction of Si with the metal M to form an inactive SiM matrix. However, the behavior of Si-Mn thin film libraries differs from that of Si-Fe and Si-Cr-Ni libraries for the range of 50–70 at% Si. The existing phases in the sputtered Si-Mn system and their activity toward lithiation/delithiation are still unclear. What's more, the results of sputtering do not always reflect what is formed during ball milling.[12] According to the Mn-Si equilibrium phase diagram (Figure 1),[21] silicon and manganese form the $Mn_{11}Si_{19}$ and MnSi phases in the 0 - 50 at% Mn composition range. The $Mn_{11}Si_{19}$ phase has the complex $Cr_{11}Ge_{19}$ structure,[22] which is unique among the transition metal silicides. The complexity of the phase formation in the Si-Mn system compared to the other Si-TM systems makes its performance in Li cells interesting to investigate and to compare with other Si-TM alloys.

In the present study, a systematic investigation of the Mn-Si system has been undertaken. $Si_{1-x}Mn_x$ ($0 \leq x \leq 0.5$, $\Delta x = 0.05$) alloys were prepared by mechanical milling and were evaluated as negative electrode materials in Li cells. The effects of composition, phase formation and structures on the electrochemical behavior were determined.

Experimental

$Si_{1-x}Mn_x$ ($0 \leq x \leq 0.5$, $\Delta x = 0.05$) alloys were prepared by SPEX milling. A total of 0.5 mL of silicon powder (Sigma-Aldrich, −325 mesh, 99%) and manganese powder (Alfa Aesar, −325 mesh, 99.95%) were loaded into 65 ml hardened steel vials (SPEX) in stoichiometric ratios. The sample vials were sealed in an Ar atmosphere. Duplicate samples were milled simultaneously in a SPEX 8000D dual mixer mill for 4 hours under the optimal milling conditions as described in Reference,[23] with the vial positions being switched at 2 hour intervals during milling. Although ball milling was conducted at room temperature, the surface temperature of the milling vials was observed to increase with milling time, reaching a maximum temperature of ∼160°C. After milling, the powders were recovered from the vials by ethyl alcohol and dried in air at 120°C for 2 hrs.

X-ray diffraction patterns were collected using a Rigaku Ultima IV diffractometer equipped with a diffracted beam graphite monochromator and using Cu K-alpha radiation. Each XRD scan was collected from 20° to 90° 2-theta in 0.05° increments for 3 seconds per step. True sample densities were measured with He gas using a Micromeritics AccuPyc II 1340 gas pycnometer. Specific surface area was determined by the single-point BET method using a Micromeritics Flowsorb II2300 surface area analyzer.
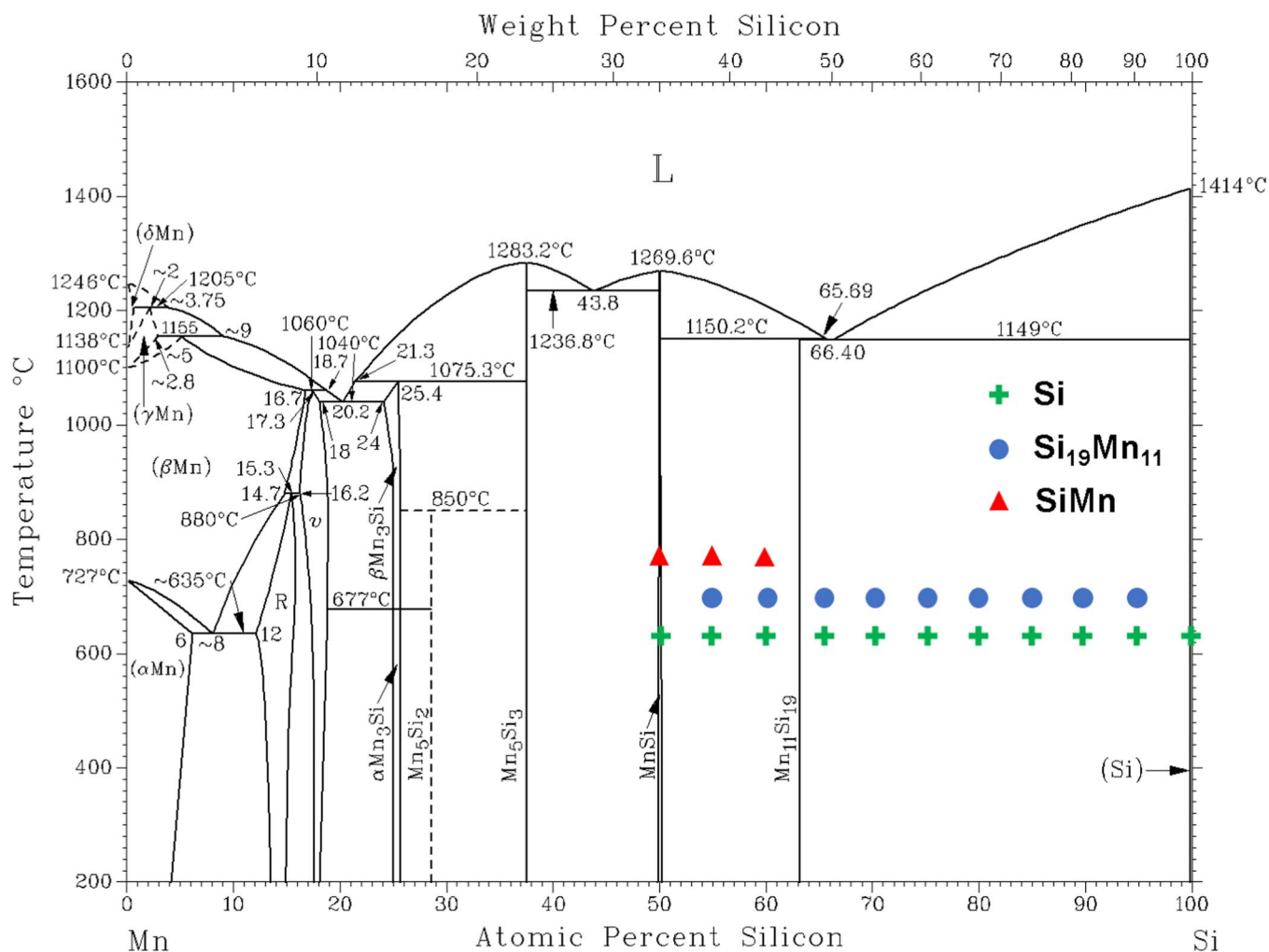
Figure 1. Phase diagram of Mn-Si system.[21] Superimposed on the phase diagram are symbols indicating the phases observed by XRD in samples prepared by ball milling at room temperature at each composition. These symbols represent the composition of the ball milled samples only and do not reflect the temperature of the ball milling process. Phase diagram reprinted from Reference 21, Copyright 1991, with permission from Springer Nature.

The samples were dispersed on carbon tape for SEM observation. Morphology of the alloys were obtained with a TESCAN MIRA 3 LMU Variable Pressure Schottky Field Emission Scanning Electron Microscope (SEM). Transmission electron microscope (TEM) images were taken using a Philips CM30 TEM. TEM specimens were made by suspending as-received powder in methanol, sonicating 10 min, and placing a drop onto a lacey carbon coated TEM grid.

Electrode slurries were prepared by mixing Si-Mn alloys, carbon black (Imerys Graphite and Carbon, Super C65) and a 10 weight % aqueous solution of lithium polyacrylate (LiPAA) with a volumetric ratio of 70/5/25 in distilled water. Slurries were mixed for one hour in a Retsch PM200 planetary mill at 100 rpm with three 13 mm tungsten carbide balls and then spread onto copper foil (Furukawa Electric, Japan) with a 0.004 inch gap coating bar. Then the coatings were dried in air for 1 hour at 120°C and cut into 1.3 cm disks and then heated under Ar for 1 hour at 120°C with no further air exposure.

Electrodes were assembled in 2325-type coin cells with a lithium foil counter/reference electrode. Two layers of Celgard 2300 separator were used in each coin cell. 1 M $LiPF_6$ (BASF) in a solution of ethylene carbonate, diethyl carbonate and monofluoroethylene carbonate (volume ratio 3:6:1, all from BASF) was used as electrolyte. Cell assembly was carried out in an Ar-filled glove box. Cells were cycled galvanostatically at 30.0 ± 0.1°C between 5 mV and 0.9 V using a Maccor Series 4000 Automated Test System. For the 1st cycle, the electrodes were lithiated at a current of C/20 and held at 5 mV until

the current decayed to a value of C/40 (trickle) and delithiated at C/20 until a 0.9 V cutoff was reached. In subsequent cycles, the electrodes were lithiated/delithiated at C/5 with a C/20 trickle discharge (lithiation). This cycling protocol was chosen to simulate conditions during cycling in a commercial Li-ion cells, as described in Reference.[24]
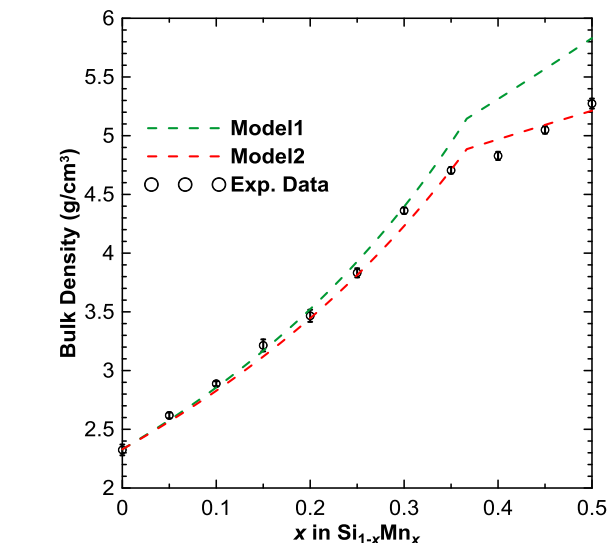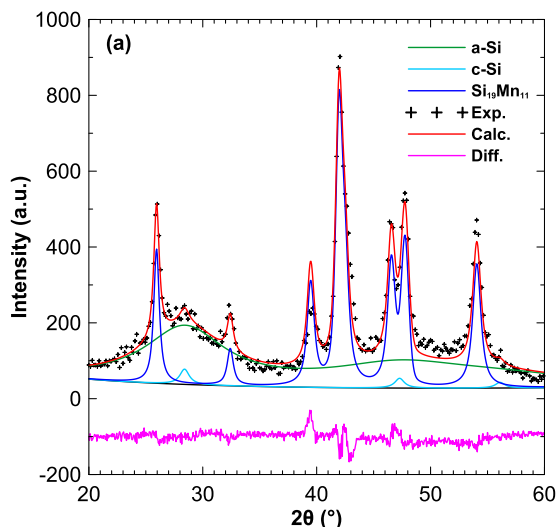
Results and Discussion

The compositions made in the $Si_{1-x}Mn_x$ sample series for this study are shown in Figures 1. Figures 2a and 2b show XRD patterns of $Si_{1-x}Mn_x$ samples with $0 \leq x \leq 0.25$ and $0.3 \leq x \leq 0.5$, respectively. The XRD peak locations and intensities are indicated for Si (PDF# 00-077-2111) and $Si_{19}Mn_{11}$ (PDF# 00-089-2629). In order to understand phase behavior in greater detail, the intensity of each phase in the samples were measured by fitting the XRD patterns using Pseudo-Voigt peak functions. An example of such a fit ($Si_{0.85}Mn_{0.15}$) is shown in Figure 3a. In the fits, the integrated peak area ratios of each phase were fixed to those found in the ICSD database. Lattice constants of each phase were allowed to vary, which determined peak positions. The Si peak was found to comprise a crystalline (c-Si) component and an amorphous (a-Si) component, as has been observed before for ball milled Si.[23] The fitting results are shown in Figure 3b and qualitatively show how the relative amount of each phase changes with Mn content. The error bars shown were estimated by noting that the changes in composition (and relative intensity) in 2-phase regions
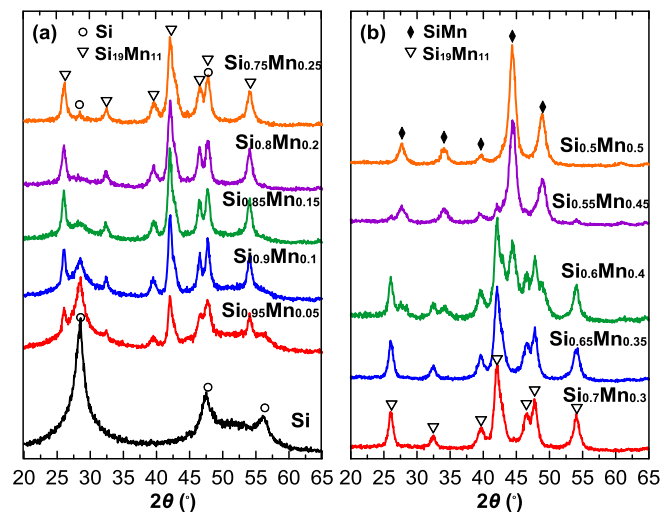
Figure 2. XRD patterns of ball milled $Si_{1-x}Mn_x$ alloys: (a) $0 \leq x \leq 0.25$, (b) $0.3 \leq x \leq 0.5$.

Figure 4. Dependence of bulk density on x in $Si_{1-x}Mn_x$ alloys. Model 1 is the predicted alloy density based on the bulk densities of the crystalline phases present. Model 2 is a fit to the data assuming the presence of voids and/or vacancies.

should be linear. Therefore, deviations from this linearity were taken as a measure of the random error. The X-ray pattern of pure silicon after ball milling shows features of amorphous and nanostructured silicon. For $0.05 \leq x \leq 0.25$, Si and $Si_{19}Mn_{11}$ coexist. With increasing Mn content, the intensity of the Si XRD peaks decreases and the peaks corresponding to the $Si_{19}Mn_{11}$ phase increase, indicating 2-phase coexistence. Additionally, the c-Si phase content becomes zero when x is greater than 0.2. At higher Mn contents, Si only exists in the amorphous phase. At compositions above $x = 0.35$ the a-Si peak becomes so small and broad that it is impossible to distinguish from the background. From the linear decrease in Si content with increasing Mn, it is likely that no free Si exists for $x > 0.35$. At higher Mn contents, XRD peaks corresponding to SiMn (PDF#96-901-3972) are observed and the XRD peaks of the $Si_{19}Mn_{11}$ phase gradually disappears, indicating a $Si_{19}Mn_{11}$-SiMn 2-phase region. Pure SiMn phase forms for the composition with $x = 0.5$. The phases observed by XRD at each composition are shown superimposed on the phase diagram in Figure 1. There is good agreement with the phase diagram.

The bulk density of the samples has a strong dependence on the manganese content, as shown in Figure 4. Dashed green lines

(Model 1) in Figure 4 represent the theoretical alloy bulk density according to the equilibrium phase diagram and using 2.285 g/ml, 5.145 g/ml, and 5.831 g/ml as the theoretical densities of Si, $Mn_{11}Si_{19}$, and MnSi, respectively. For $x \leq 0.35$, the density trend of the ball milled alloys agrees well with the theoretical density, further confirming that the equilibrium phase diagram is followed during milling. For $x \geq 0.4$, deviations toward higher density of the theoretical model increase with increasing Mn content, although the overall trend is similar to the theoretical line. Therefore, in these samples the density of the ball milled phases is less than predicted from XRD phase identification. The XRD pattern shows that there is no peak shifts or missing peaks of the SiMn and $Si_{19}Mn_{11}$ phases in all the samples. Therefore, the low observed density is likely from defects, as voids and vacancies in the alloys introduced by the ball milling process. Such effects have been shown previously to reduce the density of ball milled alloys from their bulk values.[25–27] To estimate the amount of vacancies or voids present, a stoichiometric vacancy concentration was estimated by the least squares fitting method (Model 2 in Figures 4). The
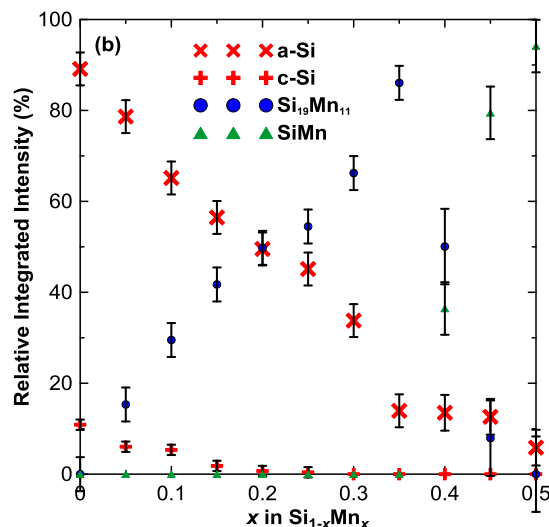
Figure 3. (a) XRD profile fitting results of $Si_{0.85}Mn_{0.15}$, (b) Relative integrated XRD intensity of different phases in $Si_{1-x}Mn_x$ alloys.
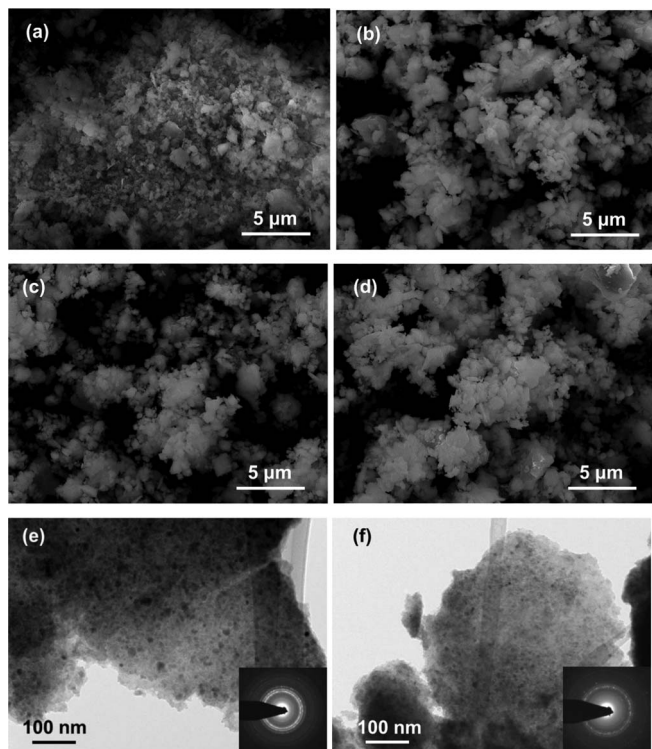
Figure 5. SEM images of Si (a), $Si_{0.7}Mn_{0.3}$ (b), $Si_{0.6}Mn_{0.4}$ (c) and $Si_{0.5}Mn_{0.5}$ (d), and TEM images of $Si_{0.7}Mn_{0.3}$ (e) and $Si_{0.6}Mn_{0.4}$ (f). The inserted figures in (e) and (f) are SAD patterns enclosing most of the bottom of the thin area shown in corresponding TEM images.
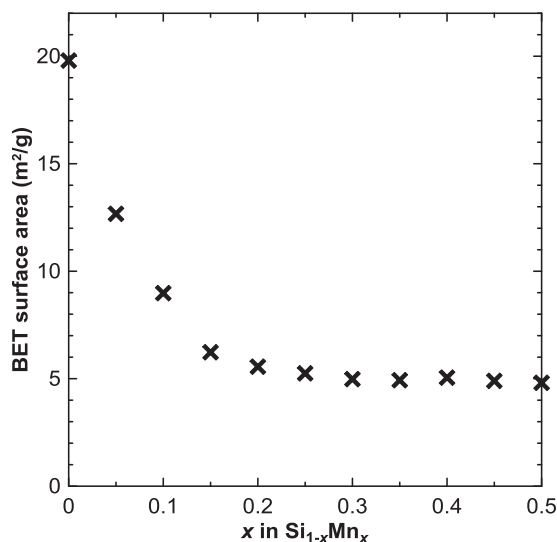
Figure 6. BET surface area of the $Si_{1-x}Mn_x$ alloys.

result from this model is a vacancy/void concentration corresponding to $(Si_{18.05\pm0.02}\square_{0.95\pm0.02})(Mn_{10.45\pm0.02}\square_{0.55\pm0.02})$ for $Si_{19}Mn_{11}$ and $(Si_{0.89\pm0.03}\square_{0.11\pm0.03})(Mn_{0.89\pm0.03}\square_{0.11\pm0.03})$ in SiMn.

Representative SEM images of the $Si_{1-x}Mn_x$ samples are shown in Figures 5a–5d. The pure Si sample particles, shown in Figure 5a, are smaller than 1 μm, with most of the particles being smaller than 0.5 μm. The addition of Mn in the sample increases the particle size, as shown in Figures 5b–5d. Correspondingly, the surface area of the samples decreases dramatically from 19.8 m²/g for pure Si to ~5 m²/g with increasing Mn content, as shown in Figure 6. There are more particles existing as flakes in Si-Mn alloys compared to pure Si, how-

ever, no obvious difference in morphology or surface area is observed among samples when the Mn content is larger than 20%. Figures 5e and 5f show TEM images of $Si_{0.7}Mn_{0.3}$ and $Si_{0.6}Mn_{0.4}$, respectively. The alloys appear to be essentially homogeneous with 10–20 nm nanocrystalline grains uniformly dispersed in an amorphous matrix of Si. In order to identify the nanocrystalline phase, selected area aperture enclosing most of the area shown in the TEM images (beam diameter is ~150 nm) was used, and the selected area diffraction patterns are shown in the inserted figures in Figures 5e and 5f. Strong diffraction rings indicate the sampled area is polycrystalline and indexing coincided with the $Si_{19}Mn_{11}$ phase for the $Si_{0.7}Mn_{0.3}$ alloy and a mixture of $Si_{19}Mn_{11}$ and SiMn for the $Si_{0.6}Mn_{0.4}$ alloy, consistent with XRD results. EDS analysis indicated that the composition of the particles is very uniform (within the resolution of the instrument) and the compositions were identified to be $Si_{0.70\pm0.05}Mn_{0.31\pm0.05}$ and $Si_{0.61\pm0.05}Mn_{0.39\pm0.05}$ for $Si_{0.7}Mn_{0.3}$ and $Si_{0.6}Mn_{0.4}$, respectively (i.e., within 1% of the desired composition). Similar results were observed for all the other samples. From these results, the $Si_{1-x}Mn_x$ ($0 \leq x \leq 0.5$) alloys consists of 1 μm particles for $x = 0$ and have larger particle sizes and substantially lower surface areas as the Mn content is increased. The particles themselves consist of 10–20 nm nanocrystalline grains of $Si_{19}Mn_{11}$ and/or SiMn uniformly dispersed in an amorphous Si matrix.

Figure 7 shows the voltage curves of $Si_{1-x}Mn_x$ alloy electrodes. Corresponding differential capacity curves are shown in Figure 8. For pure silicon, the lithiation voltage curve comprises a small plateau at about 0.27 V, which likely corresponds to a nucleation/growth mechanism for the initial lithiation. This is followed by two sloping plateaus, which are characteristic of amorphous Si. The subsequent delithiation comprises a large voltage plateau and a corresponding large peak in differential capacity at about 0.45 V, which can be attributed to the delithiation of $Li_{15}Si_4$. For $Si_{1-x}Mn_x$ alloys, only features corresponding to silicon are observed. This is consistent with these alloys being composed of an active Si phase and an inactive Mn-silicide phase, which is typical of most Si-transition metal alloys. In this case the inactive silicides correspond to those observed by XRD and TEM studies, i.e. $Si_{19}Mn_{11}$ and SiMn, as is further confirmed below.

As the Mn content is increased, the alloy capacity decreases and the peak in differential capacity curves (Figure 8) corresponding to the delithiation of $Li_{15}Si_4$ becomes less pronounced, indicating that the addition of Mn results in the suppression of $Li_{15}Si_4$ formation during lithiation. Between the composition of $Si_{0.85}Mn_{15}$ and $Si_{0.8}Mn_{0.2}$ there is a marked reduction in the $Li_{15}Si_4$ delithiation peak. For $Si_{0.8}Mn_{0.2}$, the $Li_{15}Si_4$ formation is fully suppressed during initial cycles, as shown in Figure 8e. However, as cycling progresses, the $Li_{15}Si_4$ peak appears after cycle 2 in this composition and grows during cycling. At the same time, the two broad lithiation peaks shift toward higher voltage. This suggests that the $Li_{15}Si_4$ phase is suppressed due to compressive stress from the inactive phase, which is further verified below. The shift of the lithiation peaks to higher voltage is consistent with less compressive stress is being applied to the active Si phase as cycling progresses. This would occur if the Si phase is debonding from the $Si_{19}Mn_{11}$ inactive phase during cycling (i.e. particle fracture). As the Mn content is increased further to 30%, the formation of $Li_{15}Si_4$ is completely suppressed for all 50 cycles and little change is seen in the differential capacity curve. This is likely the minimum Mn content required to enable longer term cycling.

Curiously, compositions above 40% Mn content show large peaks due to $Li_{15}Si_4$ delithiation. However, the capacity of these compositions is very small. Theoretically, the 50% Mn composition should not contain any elemental Si. Therefore, the capacity observed must be due to a small amount of unreacted elemental Si powder. This powder may have been trapped in the corners of the milling vessel during the milling process. It is likely that this small amount of unreacted Si is present in all samples, but its capacity is too small to be noticed in the samples with lower Mn content.

Figure 9 shows the average second lithiation/delithiation voltage and polarization of $Si_{1-x}Mn_x$ alloys as a function of composition.
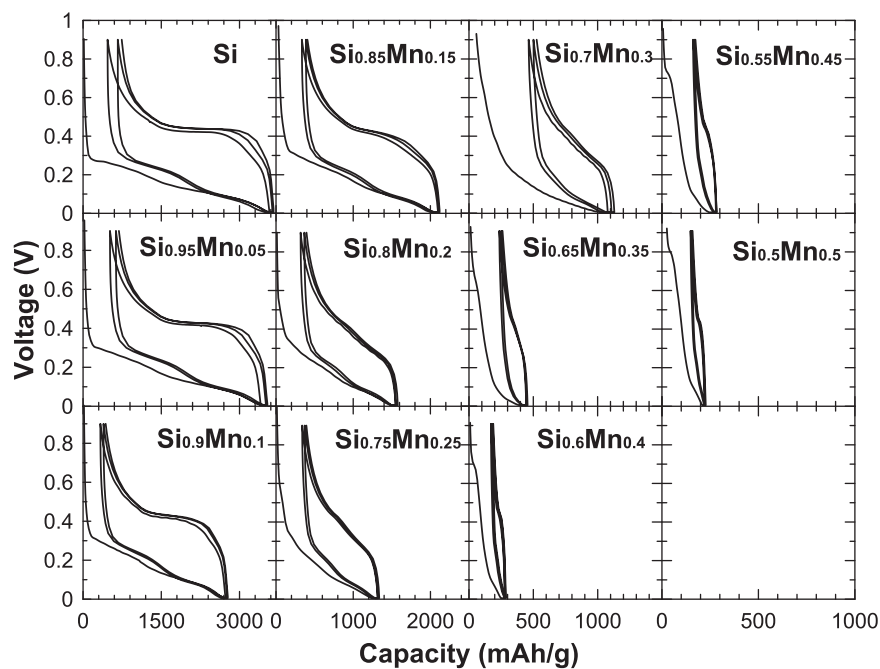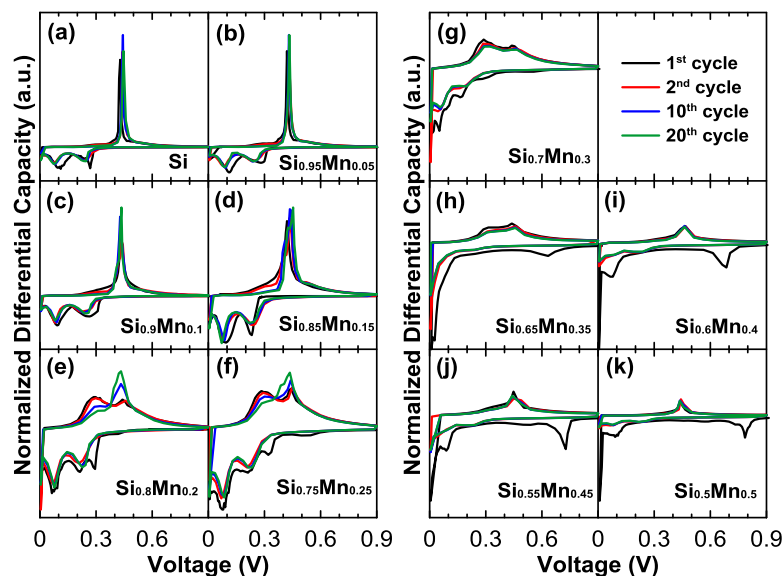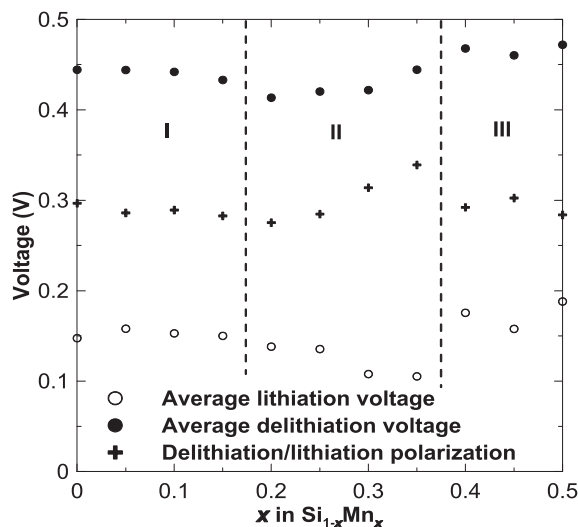
Figure 7. Voltage curves of $Si_{1-x}Mn_x$ alloys.

Figure 8. Differential capacity curves of $Si_{1-x}Mn_x$ alloy electrodes derived from Figure 7 for the 1st (black), 2nd (red), 10th (blue) and 20th (green) cycles.

Three regions are apparent in the figure. In Region I ($x < 0.2$), the Mn content is small and the lithiation and delithiation voltage remain relatively constant. This is consistent with the differential capacity results above, which show that the formation of $Li_{15}Si_4$ is not appreciably suppressed. In Region II ($0.2 \leq x \leq 0.35$), the average delithiation voltage begins to be significantly changed by the addition of Mn and decreases with increasing Mn content. The depressed lithiation voltage results in the suppression of the $Li_{15}Si_4$ phase.[28] These trends in voltage are consistent with compressive stress from the inactive silicide phase being applied to the active Si phase in the alloy during lithiation, while any large tensile stresses during delithiation are relieved by particle fracture.[10] The combination of a decreasing lithiation voltage and a relatively stable delithiation average voltage results in an overall increase in cell polarization. In Region III ($0.35 \leq x \leq 0.5$), the alloy is essentially inactive (see Figure 10 and related discussion below). As mentioned above, the only electrochemical activity in this region is from an unreacted Si phase. Therefore, the average voltage is that of unconstrained elemental Si.

Figure 10 shows the first delithiation capacity of $Si_{1-x}Mn_x$ alloys as a function of Mn content. Also shown in Figure 10 is the alloy theoretical capacity calculated assuming that all the Mn in the alloy reacts with Si to form inactive $Mn_{11}Si_{19}$ or MnSi phases, according to the XRD and TEM results and that any residual silicon not incorporated in an Si-Mn silicide phase can alloy with 3.75 Li.[8] Based on these assumptions, the capacity of $Si_{1-x}Mn_x$ alloys is 0 when no residual elemental Si exists, i.e. corresponding to a composition of $Si_{19}Mn_{11}$ (x = 0.367). The measured capacity of $Si_{1-x}Mn_x$ alloys agrees well with this model, demonstrating that both $Si_{19}Mn_{11}$ and SiMn are inactive phases toward lithiation/delithiation. This is in contrast with $NiSi_2$ and Cu_3Si phases, which have been found to be electrochemically active.[29,30] These results are consistent with the differential capacity curves shown in Figure 8, which are characteristic of only a Si phase being active.

Figure 11a shows the specific capacity of $Si_{1-x}Mn_x$ alloys versus cycle number for $x < 0.35$. The cycle 10–50 capacity retention for these alloys is shown in Figure 11b. For $x = 0$ (i.e. pure Si), the electrode has significant capacity fade, resulting in the lowest capacity

Figure 9. Average second lithiation and delithiation voltages of $Si_{1-x}Mn_x$ alloys versus x.
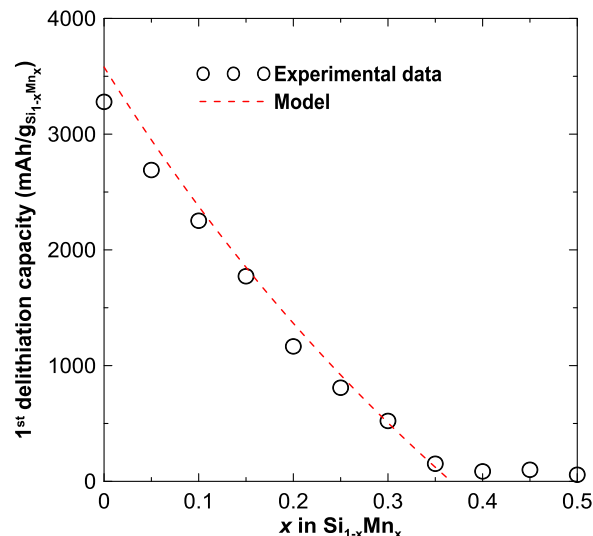
Figure 10. Dependence of 1st delithiation capacity on Mn content in $Si_{1-x}Mn_x$. Circles: experimental data calculated from the electrochemical cycling test, dashed line: theoretical data calculated by assuming silicon is the only active phase in the alloy.

retention. This can be attributed to the large volume expansion of pure Si and the 2-phase region associated with $Li_{15}Si_4$ formation, which is believed to cause internal particle fracture.[2] Increasing the Mn content results in lower volume expansion and reduced fade. Capacity retention is maximized at a value of 96.8% at a composition of $x = 0.25$. This also corresponds to the composition at which $Li_{15}Si_4$ formation becomes nearly fully suppressed (Figure 8). For $x \geq 0.3$, all the samples have similar cycling performance. Good cycling in these alloys is attributed to a reduced volume expansion and the absence of $Li_{15}Si_4$ phase formation.

Figure 12 shows the volumetric capacity calculated at full volume expansion and the volume expansion of $Si_{1-x}Mn_x$ alloys. These values were calculated based on lithium occupying 8.9 mL/mol in Si alloys.[1] Both volumetric capacity and volume expansion are reduced with increasing x, as expected. Compositions at which volume expansion is reduced and $Li_{15}Si_4$ formation is fully suppressed in order to obtain good cycling performance are those with $x \geq 0.25$, as discussed above. Such alloys can have volumetric capacities up to 1500 Ah/L and an average delithiation voltage of about 0.43 V. Based on these values, when utilized in Li-ion cell such alloys could theoretically provide an

increase in volumetric energy of up to 25% as compared to a baseline $LiCoO_2$/graphite cell, according to the cell stack model in Reference 2.

Conclusions

$Si_{1-x}Mn_x$ alloys were prepared over a large composition range ($0 \leq x \leq 0.5$) by ball milling. The alloys comprise particles > 1 μm in size in which 10–20 nm nanocrystalline grains of $Si_{19}Mn_{11}$ and/or SiMn are uniformly dispersed in an amorphous Si matrix. The addition of Mn increases the particle size, resulting in significantly reduced surface area. All these alloys have voltage curves typical of amorphous Si and their capacities are consistent with the $Si_{19}Mn_{11}$ and SiMn phases being electrochemically inactive. However, with increasing Mn content, the lithiation voltage was decreased, resulting in the suppression of $Li_{15}Si_4$ formation during cycling for $x \geq 0.3$. This composition also coincided with maximized capacity retention. These results demonstrate that Mn can suppress $Li_{15}Si_4$ formation, resulting
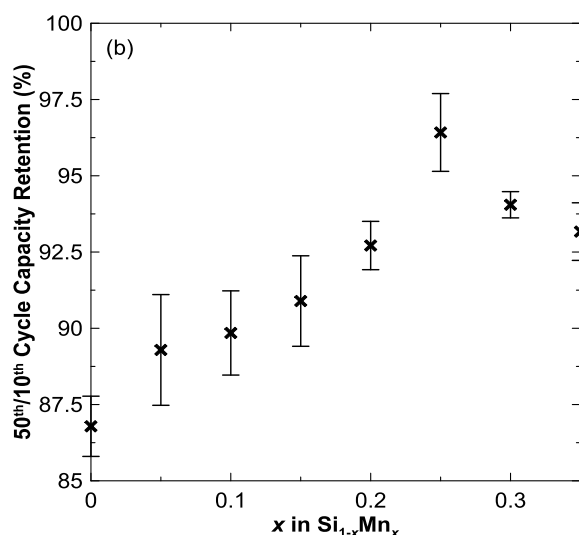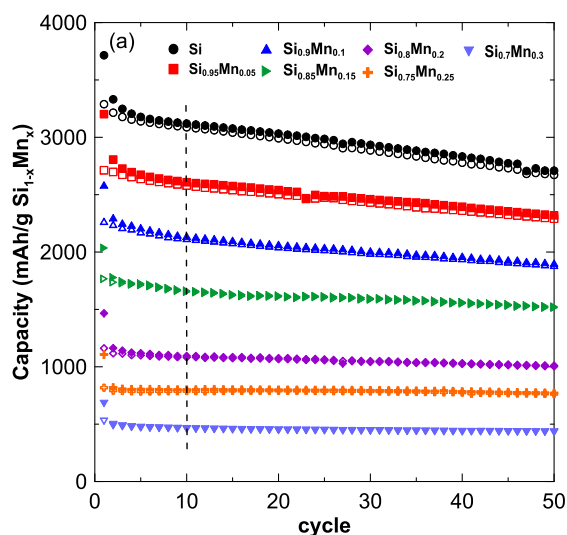
Figure 11. (a) The lithiation (closed symbols) and delithiation (open symbols) capacities of ball milled $Si_{1-x}Mn_x$ alloys versus cycle number and (b) the capacity retention versus Mn content.
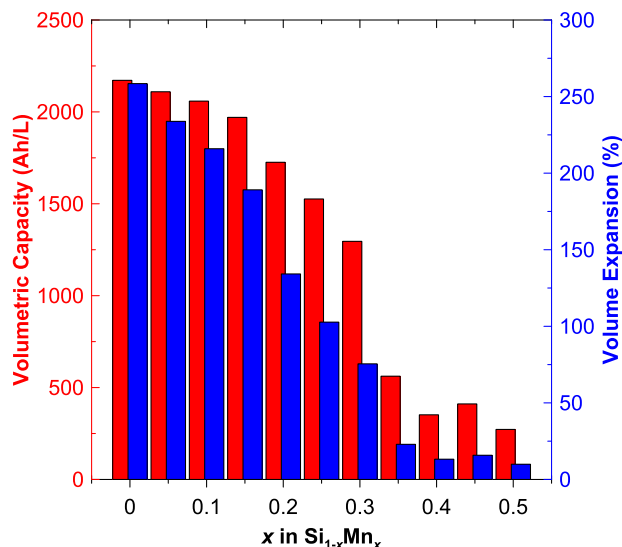
Figure 12. Volumetric capacity and volume expansion of ball milled $Si_{1-x}Mn_x$ alloys versus x.

in good capacity retention at compositions having high volumetric capacity (>1500 Ah/L).

ORCID

M. N. Obrovac ⓘ https://orcid.org/0000-0001-5509-3185

References

1. M. N. Obrovac, L. Christensen, D. B. Le, and J. R. Dahn, "Alloy Design for Lithium-Ion Battery Anodes," *J. Electrochem. Soc.*, **154**, A849 (2007).
2. M. N. Obrovac and V. L. Chevrier, "Alloy Negative Electrodes for Li-Ion Batteries M. N. Obrovac," *Chem. Rev.*, **114**, 11444 (2014).
3. M. N. Obrovac and L. Christensen, "Structural Changes in Silicon Anodes during Lithium Insertion/Extraction," *Electrochem. Solid-State Lett.*, **7**, A93 (2004).
4. B. Jerliu, E. Hüger, L. Dörrer, B. K. Seidlhofer, R. Steitz, V. Oberst, U. Geckle, M. Bruns, and H. Schmidt, "Volume expansion during lithiation of amorphous silicon thin film electrodes studied by in-operando neutron reflectometry," *J. Phys. Chem. C.*, **118**, 9395 (2014).
5. N. Liu, Z. Lu, J. Zhao, M. T. McDowell, H.-W. Lee, W. Zhao, and Y. Cui, "A pomegranate-inspired nanoscale design for large-volume-change lithium battery anodes," *Nat. Nanotechnol.*, **9**, 187 (2014).
6. T. D. Hatchard, M. N. Obrovac, and J. R. Dahn, "Electrochemical Reaction of the Si[sub 1−x]Zn[sub x] Binary System with Li," *J. Electrochem. Soc.*, **152**, A2335 (2005).
7. T. D. Hatchard and J. R. Dahn, "Study of the Electrochemical Performance of Sputtered Si[sub 1−x]Sn[sub x] Films," *J. Electrochem. Soc.*, **151**, A1628 (2004).
8. M. D. Fleischauer, J. M. Topple, and J. R. Dahn, "Combinatorial Investigations of Si-M (M = Cr + Ni, Fe, Mn) Thin Film Negative Electrode Materials," *Electrochem. Solid-State Lett.*, **8**, A137 (2005).
9. T. D. Hatchard, M. N. Obrovac, and J. R. Dahn, "Electrochemical Reaction of the SiAg Binary System with Li," *J. Electrochem. Soc.*, **152**, A1445 (2005).
10. Z. Du, T. D. Hatchard, R. A. Dunlap, and M. N. Obrovac, "Combinatorial Investigations of Ni-Si Negative Electrode Materials for Li-Ion Batteries," *J. Electrochem. Soc.*, **162**, A1858 (2015).
11. S. Kirklin, B. Meredig, and C. Wolverton, "High-throughput computational screening of new Li-Ion battery anode materials," *Adv. Energy Mater.*, **3**, 252 (2013).
12. Z. Du, S. N. Ellis, R. A. Dunlap, and M. N. Obrovac, "Ni x Si 1-x Alloys Prepared by Mechanical Milling as Negative Electrode Materials for Lithium Ion Batteries," *J. Electrochem. Soc.*, **163**, A13 (2015).
13. H. Usui, K. Meabara, K. Nakai, and H. Sakaguchi, "Anode properties of composite thick-film electrodes consisted of Si and various metal silicides," *Int. J. Electrochem. Sci.*, **6**, 2246 (2011).
14. H.-Y. Lee and S.-M. Lee, "Graphite–FeSi alloy composites as anode materials for rechargeable lithium batteries," *J. Power Sources.*, **112**, 649 (2002).
15. M.-S. Park, Y.-J. Lee, S. Rajendran, M.-S. Song, H.-S. Kim, and J.-Y. Lee, "Electrochemical properties of Si/Ni alloy–graphite composite as an anode material for Li-ion batteries," *Electrochim. Acta.*, **50**, 5561 (2005).
16. Y. S. Lee, J. H. Lee, Y. W. Kim, Y. K. Sun, and S. M. Lee, "Rapidly solidified Ti-Si alloys/carbon composites as anode for Li-ion batteries," *Electrochim. Acta.*, **52**, 1523 (2006).
17. M. D. Fleischauer, R. Mar, and J. R. Dahn, "Method to Predict Phase Formation and Specific Capacity for Lithium in Codeposited Silicon-Transition Metal Thin Films," *J. Electrochem. Soc.*, **154**, A151 (2007).
18. P. Zuo and G. Yin, "Si-Mn composite anodes for lithium ion batteries," *J. Alloys Compd.*, **414**, 265 (2006).
19. P. Zuo, G. Yin, and Y. Tong, "SiMn-Graphite composites as anodes for lithium ion batteries," *Solid State Ionics.*, **177**, 3297 (2006).
20. M. D. Fleischauer and J. R. Dahn, "Combinatorial Investigations of the Si-Al-Mn System for Li-Ion Battery Applications," *J. Electrochem. Soc.*, **151**, A1216 (2004).
21. H. Okamoto, "Mn-Si (Manganese-Silicon)," *J. Phase Equilibria.*, **12**, 505 (1991).
22. N. J. Ghimire, M. A. McGuire, D. S. Parker, B. C. Sales, J. Q. Yan, V. Keppens, M. Koehler, R. M. Latture, and D. Mandrus, "Complex itinerant ferromagnetism in noncentrosymmetric Cr 11Ge 19," *Phys. Rev. B - Condens. Matter Mater. Phys.*, **85**, 1 (2012).
23. T. D. Hatchard, A. Genkin, and M. N. Obrovac, "Rapid mechanochemical synthesis of amorphous alloys," *AIP Adv.* **7**, (2017).
24. V. L. Chevrier, L. Liu, D. B. Le, J. Lund, B. Molla, K. Reimer, L. J. Krause, L. D. Jensen, E. Figgemeier, and K. W. Eberman, "Evaluating Si-Based Materials for Li-Ion Batteries in Commercially Relevant Negative Electrodes," *J. Electrochem. Soc.*, **161**, A783 (2014).
25. B. Q. Zhang, L. Lu, and M. O. Lai, "Evolution of vacancy densities in powder particles during mechanical milling," *Phys. B Condens. Matter.*, **325**, 120 (2003).
26. Y. Wang, S. Cao, M. Kalinina, L. Zheng, L. Li, M. Zhu, and M. N. Obrovac, "Lithium Insertion in Nanostructured $Si_{1-x}Ti_x$ Alloys," *J. Electrochem. Soc.*, **164**, A3006 (2017).
27. Z. H. Yan, M. Oehring, and R. Bormann, "Metastable phase formation in mechanically alloyed and ball milled Ti-Si," *J. Appl. Phys.*, **72**, 2478 (1992).
28. D. S. M. Iaboni and M. N. Obrovac, "Li15Si4 Formation in Silicon Thin Film Negative Electrodes," *J. Electrochem. Soc.*, **163**, A255 (2016).
29. Z. Du, T. D. Hatchard, P. Bissonnette, R. A. Dunlap, and M. N. Obrovac, "Electrochemical Activity of Nano-NiSi2 in Li Cells," *J. Electrochem. Soc.*, **163**, A2456 (2016).
30. Z. Du, H. Liu, S. N. Ellis, R. A. Dunlap, M. Zhu, and M. N. Obrovac, "Electrochemistry of Cu_xSi_{1-x} Alloys in Li Cells," *J. Electrochem. Soc.*, **163**, A1275 (2016).